



# A gas cell for thermalizing, storing and transporting radioactive ions and atoms. Part I: Off-line studies with a laser ion source

Yu. Kudryavtsev<sup>\*</sup>, B. Bruyneel, M. Huyse, J. Gentens, P. Van den Bergh, P. Van Duppen, L. Vermeeren<sup>1</sup>

*Instituut voor Kern- en Stralingsfysika, University of Leuven, Celestijnenlaan 200 D, B-3001 Leuven, Belgium*

Received 25 January 2001

---

## Abstract

The application of a gas cell filled by noble gas (He or Ar) for thermalizing, storing and transporting trace radioactive ions and atoms has been studied in off-line conditions. Two-step laser resonance ionization has been used to produce ions of stable and long-lived radioactive isotopes inside the cell. The interactions of ions with impurity molecules, with noble gas atoms, with electrons and with electrical fields have been investigated in order to specify the requirements for the gas cell as a source of radioactive rare isotopes for the next generation radioactive ion beam facilities. Extraction and transport of ions by the sextupole ion guide (SPIG) without applying DC electrical field allows to get information about the gas purity and about chemical reactions which take place inside the gas cell. © 2001 Elsevier Science B.V. All rights reserved.

*PACS:* 29.25; 32.80.F6; 41.85.Ar

*Keywords:* Gas cell; Laser resonance ionization; Ion guide

---

## 1. Introduction

In the study of exotic nuclei far from stability at on-line isotope separators the target-catcher-ion source system should be universal, in order to produce beams of all elements of the table of

Mendeleejev; it should be fast, in order to minimize decay losses of the shortest living species and it should be element-selective, in order to separate the rare nuclei of a particular element from the more stable isobaric contaminants, which are typically orders of magnitude more produced in the used nuclear reactions. The radioactive isotopes are produced in a target and thermalized in the catcher. Two possible catcher systems can be used: a solid- or liquid-catcher where the radioactive isotopes diffuse out by heat and a gaseous-catcher where the produced nuclei are transported by gas flow and/or by electrical fields. The first

---

<sup>\*</sup> Corresponding author. Tel.: +32-16-32-72-70; fax: +32-16-32-79-85.

*E-mail address:* yuri.kudryavtsev@fys.kuleuven.ac.be (Y. Kudryavtsev).

<sup>1</sup> Present address. SCK-CEN, Boeretang 200, B-2400 Mol, Belgium.

solution can easily be integrated with thick targets and different types of ion sources. Element selectivity can for a number of elements be achieved as the release time in such a target-catcher-ion source system is governed by the chemical properties of the element studied. The drawback of this approach is that for certain elements (B, S, Si, P and the transition elements in the groups 5B, 6B, 7B and 8) severe losses do occur due to their refractory nature and that even for the most volatile elements it is hard to reduce the release time below some 10 ms. The gas-catcher can form an alternative, as it is fast and universal, but its integration with a thick production target and with an ion source is problematic. This has to do with different loss processes in the gas cell and with the conflicting combination of a high gas load and a highly efficient hot ion source. A partial way out is to evacuate the radioactive species in their ionic form as applied in the ion guide isotope separation on line (IGISOL) technique. This technique has successfully been used at different on-line mass separators for nuclear structure studies on short-living nuclei even of refractory nature and has recently been reviewed by Dendooven [1]. Another possibility is to re-ionize the radioactive atoms as done with laser-induced multi-step resonance ionization at the Leuven isotope separator on line (LISOL) [2–7]. Here the nuclear reaction products recoil out of the target; they are thermalized and neutralized in a noble buffer gas, then resonantly ionized by the laser beams, extracted from the ion source, accelerated and mass separated. In this way isobaric and isotopic selectivity can be achieved. The laser ion source (LIS) made it possible to perform for the first time high-precision measurements of the  $\beta$  and  $\gamma$  decay of  $^{68-74}\text{Ni}$  [8] and  $^{66-70}\text{Co}$  [9–11]. These nuclei have been produced in proton-induced fission reactions of  $^{238}\text{U}$ . A similar approach but focused on laser spectroscopy of radioactive atoms in a gas cell has been developed at the Mainz University [12]. Both approaches, fast evacuation of thermalized ions and re-ionization of thermalized atoms, are seriously affected by the interactions, which the trace atoms and ions undergo during their transport in the buffer gas. These interactions depend strongly on the buffer gas itself, on the impurities in the gas

and on the ionization degree of the gas. Such interactions can be quantified by a characteristic time scale, which relates to chemical reaction rate constants and ion recombination rate constants. These time scales should then be compared with the transport times in the cell, induced by flow, drag or diffusion, in order to evaluate possible losses.

In order to enlarge the possibilities of a gas cell for the production of intense beams of radioactive ions as discussed for the next generation of radioactive beams, it is of crucial importance to characterize the different stages a radioactive ion undergoes in its journey through the gas cell. It starts with the recoil after the nuclear reaction into the gas cell, followed by the slowing down process till thermal energies. From then on a major role is played by the different interactions of the radioactive nucleus, in its atomic or ionic form, with the buffer gas, with impurities, with electrons and with electrical fields. In this paper we concentrate on the journey once thermal energies are reached and we describe the results of off-line experiments with stable atoms and atoms from long-lived radioactive isotopes ionized in a gas cell by laser ionization.

On-line conditions are essentially different from off-line ones. First of all a much more dense plasma can be created by the passage of the primary particle beam through the gas cell or by the slowing down process of the produced ions. A second difference consists in the fact that the produced nuclei are changing during their slowing down from multi-charged atomic ions to doubly and singly charged ions and neutral atoms. Finally, the gas cell is located in a highly radioactive area. A series of on-line experiments with the LIS have been conducted to study these effects and will be published in a consequent paper.

## 2. Experimental setup

Fig. 1 shows a general view of the LIS and its coupling to the mass separator through the sextupole ion guide (SPIG) [6]. In the present setup the skimmer electrode, using a static electrical field, has been replaced by the SPIG, which uses a

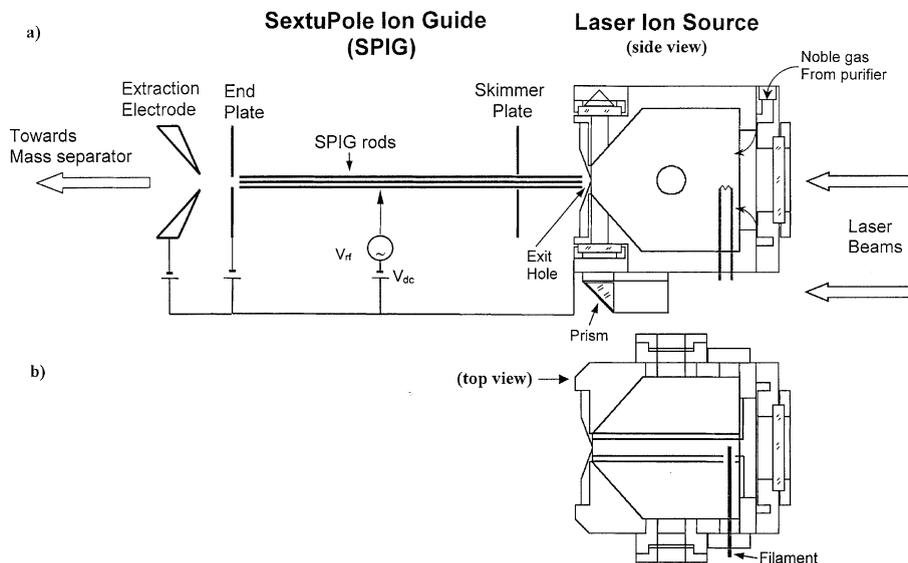


Fig. 1. (a) A side view of the LIS together with the SPIG, (b) a top view of the LIS with a 6 mm inset.

combination of static and radio frequency (RF) electrical fields to transport ions from the high-pressure zone of the gas cell to the high-vacuum zone of the mass separator. The introduction of the SPIG led to three major improvements. First of all the buffer gas pressure inside the ion source could be raised without affecting the high vacuum in the accelerating stage of the mass separator, leading to an increased stopping efficiency for energetic nuclear reaction products in on-line applications. Secondly the ion beam quality drastically improved due to the cooling capacity of the SPIG and thirdly the ion guide allowed us to study the processes of molecular ion formation and ion neutralization inside the ion source as these molecular ions can now be transported to the mass separator by the SPIG without applying a DC electrical field and consequently without destruction.

### 2.1. Laser ion source

The LIS has been optimized for on-line work where the nuclear reaction products recoil out of the target and are thermalized in the He or Ar buffer gas. They then move in the buffer gas flow towards the exit hole (see Fig. 1(a)). The inner

diameter of the ion source is equal to 5 cm. The body of the cell is made of stainless steel and is electro-polished to reduce the level of surface roughness and a possible “memory effect” of previous use. All parts of the source are sealed by indium and the whole body can be heated up to 120°C. In the off-line tests the targets are removed and the configuration of the inner part of the gas cell can be changed by putting different insets inside the cell. This allows to optimize the volume and the evacuation time of the cell for different types of studies. Atoms of different elements (Ni, Co, Cu, Rh, Ti) can be produced inside the source by resistive heating of the corresponding filament. The filaments are made from a 0.1 mm thick foil by laser cutting. The size of the hot part of the filament is  $1 \times 5 \text{ mm}^2$ . A series of off-line tests was also conducted with the long-lived  $^{57}\text{Co}$  isotope deposited on a molybdenum filament.

The laser light can enter the cell longitudinally as well as transversely. In the longitudinal case, the laser beams ionize neutral atoms along the axis of the cell. In the transverse case, a prism reflects the laser light and only atoms next to the exit hole are ionized. In the off-line experiments only the longitudinal path was used. The diameter of the laser beams inside the ion source is about 4–6 mm. The

laser optical system consists of two dye lasers pumped by two time synchronized XeCl (308 nm) excimer lasers. The laser pulse length equals 15 ns. The dye laser bandwidth equals  $0.15 \text{ cm}^{-1}$ . To get UV light, the frequency of the first step laser radiation is doubled in the second harmonic generator. The dye laser beams are directed to the ion source located at a distance of 15 m where the two laser beams are overlapped at a small angle. The maximum laser pulse repetition rate is equal to 400 Hz. The dye laser frequencies of both lasers are tuned to ionize the selected element through an autoionizing state. Table 1 shows wavelengths for the two-step laser ionization of different elements. The laser power of both lasers is high enough to saturate the atomic transitions.

The conductance of the exit hole of 0.5 mm in diameter is equal to 0.112 l/s for helium and 0.035 l/s for argon. In order to get laminar flow, the buffer gas enters the cell homogeneously through a ring slit of 0.3 mm in thickness and of 3.5 cm in diameter. Based on the dimensions and on the conductance, one can estimate that the transport time through the cell of the ions created close to the filament amounts to 500 ms in helium gas and 1500 ms in argon. This time does in first approximation not depend on the pressure inside the ion source, which ranges in our experiments from 100 to 500 mbar, but more detailed flow patterns and ion time profiles are discussed further on.

Fig. 1(b) shows the top view of the cell but with an inset, which was used for studying recombination processes in the cell after laser ionization. The inner diameter of the inset equals 6 mm. The evacuation time of the whole volume ( $1.4 \text{ cm}^3$ ) for helium as buffer gas equals 12.5 ms. The hot part of

the filament is located in the center of the channel at the distance of 49 mm from the exit hole.

## 2.2. Radio frequency ion guide

The ions leaving the gas cell are captured by the SPIG and transported towards the extraction electrode (Fig. 1(a)). The SPIG has been described in [6]. It consists of six rods (124 mm long and a diameter of 1.5 mm) cylindrically mounted on a sextupole structure with an inner diameter of 3 mm. The distance between the SPIG rods and the ion source is equal to 2 mm. An oscillating voltage  $V_{\text{rf}}$  with fixed frequency of 4.7 MHz and variable peak-to-peak amplitude of 0–500 V is applied to the rods with every rod in antiphase to the two neighboring rods. The buffer gas is pumped out efficiently through the gaps between the rods while the ions are confined and transported to the extraction electrode with the gas jet velocity. The skimmer plate separates the high-vacuum chamber of the separator and low-vacuum part around the gas jet. The main difference from the previous skimmer setup for the study of ion interactions in the gas cell consists in the fact that ions can now be guided towards the mass separator without applying a DC voltage in the high-pressure zone between the gas cell and the SPIG rods. In this case the ions are not gaining energy through the electrical field in a zone where still many collisions occur. Such energetic collisions could lead to dissociative reactions and the destruction of the molecular ions. The main acceleration of ions takes place only near the extraction electrode where a relatively high vacuum ( $10^{-5}$  Torr) is achieved. The transport efficiency through the SPIG is measured to be higher than 50%. The travel time of ions through the SPIG and mass separator was measured to be 180  $\mu\text{s}$  for helium and 300  $\mu\text{s}$  for argon. These values correspond to the jet velocity of the buffer gas. A segmentation of the SPIG rods and a consequent voltage gradient could speed up this transit time but is not implemented yet. A voltage  $V_{\text{dc}}$  (0–300 V) can be applied between the gas cell and the SPIG rods to dissociate molecular ions, which might be formed inside the cell after laser ionization. This voltage is always applied during on-line experiments in order to avoid the

Table 1  
The laser wavelengths used for the two-step ionization of Co, Cu, Ni, Rh, Ru and Ti atoms (nm)

	First step	Second step
Co	230.903	481.90
Cu	244.164	441.60
Ni	232.003	537.84
Rh	232.258	572.55
Ru	228.538	553.09
Ti	395.821	339.35

loss of ions in molecular side bands. The energy spread of ions transported by the SPIG is less than 1 eV irrespective of the applied  $V_{dc}$ . This is in sharp contrast with the previously used skimmer where a strong correlation was observed between the applied skimmer voltage and the energy spread of the beam resulting in a poor mass-resolving power [6]. The low energy spread and the good mass-resolving power using the SPIG shows the cooling capacity of the RF ion guide. However, when the distance between the SPIG and the gas cell is larger than 4 mm, this cooling capacity drops and the energy spread increases.

### 2.3. Gas handling system

The gas handling system was especially designed to supply and to control the gas flow in the gas cell. It offers also the possibility to add a known amount of another gas to the main gas line. Electro-polished stainless steel tubes and metal-sealed valves have been used in order to reduce the memory effect. The system can be heated up to 200°C and is pumped by oil-free pumps.

The scheme of the gas handling system is shown in Fig. 2. High-purity helium or argon gas (grade 6.0, 99.9999%) is supplied by Air Products and an analysis of the impurities in the gas bottle was each time provided by the manufacturer. Typically these impurities are  $H_2O$  (< 0.5 ppm),  $O_2$  (< 20 ppb),  $N_2$  (< 20 ppb). The gas is additionally purified in a getter-based purifier (MonoTorr Phase II 3000, SAES Pure Gas, Inc.) to the sub-ppb level. It is not possible to measure the impurity level inside the gas cell at this concentration. Only by adding a known amount of an

impurity gas and observing the change in the mass spectra and in the ion time profile signals it is possible to make firm conclusions. The gas flow rate in the main line (and consequently the pressure in the gas cell) is controlled by a needle valve and is measured by a digital mass flow meter (Brooks Instrument, 5860 S). The maximum flow rate is equal to 8  $l_n$ /min ( $l_n$  = normalized liter for 0°C and 1 atm). At a helium pressure inside the gas cell of 500 mbar the measured gas flow is equal to 3.7  $l_n$ /min, which is close to 3.4  $l_n$ /min calculated from the conductance of the exit hole. A small amount of impurity gas ( $O_2$ ,  $N_2$ ) can be admixed to the main gas line through a digital mass flow controller (Brooks Instrument, 5850 S). The flow rate can be varied between 0.0004 and 0.04  $l_n$ /min. A premixture of impurity gas in the noble gas in the ratio of 1:1000 was used. At a flow rate in the main line of 3.7  $l_n$ /min, the level of impurities can then be changed from 0.1 to 10 ppm. It was checked that there is no memory effect of the system for oxygen and nitrogen at this level of impurities. The most abundant impurity in the noble gas is however water vapor. The moisture concentration in the admixing gas ( $He + O_2/N_2$ ) was specified by the manufacture and equals 1.2 ppm for  $O_2$  and 0.09 ppm for  $N_2$ . This means that by adding 1 ppm of oxygen to the main line we get 1.2 ppb of  $H_2O$  in the gas cell at the noble gas pressure of 500 mbar. The corresponding value when adding nitrogen is equal to 0.09 ppb.

### 2.4. Detection

The ions produced in the gas cell and transported through the SPIG, are accelerated to an

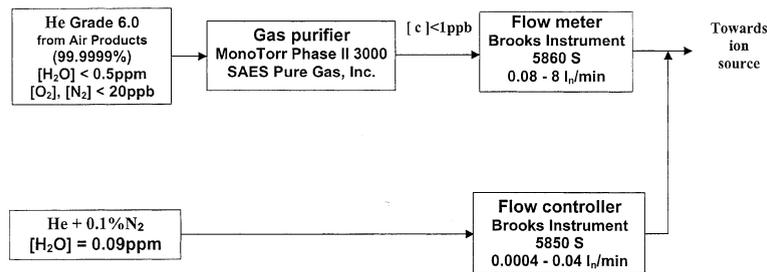


Fig. 2. Layout of the gas-handling system.

energy of 50 keV and mass separated in a 55° dipole magnet with a radius of 1.5 m. A mass resolving power of 1450 is obtained. The current of mass-separated ions is measured by a Faraday cup located in the focal plane of the mass separator. The typical laser pulse repetition rate for those measurements is equal to 30 Hz. Information on the different processes that ions undergo inside the gas cell can be obtained from the ion time profiles after longitudinal laser ionization of stable atoms. These signals are collected after mass separation by measuring the ion current through a secondary electron multiplier (SEM). By changing the acceleration voltage applied to the SEM the dynamic range of the SEM can be varied. The minimum ion current sufficient to collect time profiles lies around 0.1 fA (600 pps); the current of laser-induced ions can be changed by changing the number of available atoms vaporized by the filament (through a change of temperature).

### 3. Processes inside the gas cell

The history of an ion detected in the SEM or in the Faraday cup starts with the evaporation of an atom of interest from the filament into the buffer gas. From then on it moves with the buffer gas flow towards the exit hole. Superimposed on this flow is the diffusion process. In the many collisions with the buffer gas molecules or with impurity molecules, the atom can eventually form a chemical bond or get trapped in a metastable state which in both cases could lead to a loss for laser ionization as the used laser schemes excite only the atomic ground state. When the atoms, remaining in the atomic ground state, reach the laser interaction zone they are all ionized within one laser pulse. The laser pulse gives a time stamp with a width of about 15 ns. From here onwards the ions move further with the gas flow towards the exit hole. Their diffusion should be described by ambipolar diffusion but in this paper we will treat the diffusion process of atoms and ions on equal footing and neglect the rather small difference in diffusion coefficients. When applicable one has to take electrical fields applied in the cell into account. During their transport, the ions are col-

liding with buffer gas and impurity molecules and can interact with electrons, all this leading eventually to neutralization and thus losses of the ion signal or to formation of molecular ions. The molecular ions on their turn can recombine with electrons through the dissociative recombination leading eventually to the formation of atoms in their ground or excited state. These processes relevant to the present off-line studies are schematized in Fig. 3. The involved time scale depends essentially on the concentration of the reactants and on the reaction rate constants. In the next paragraph we describe the above-mentioned processes.

#### 3.1. Atom and/or ion–molecule reaction rates

A first type of reaction to be discussed is an association reaction of an atom X or ion  $X^+$  with a ligand molecule M in the presence of the buffer gas. For He as buffer gas,

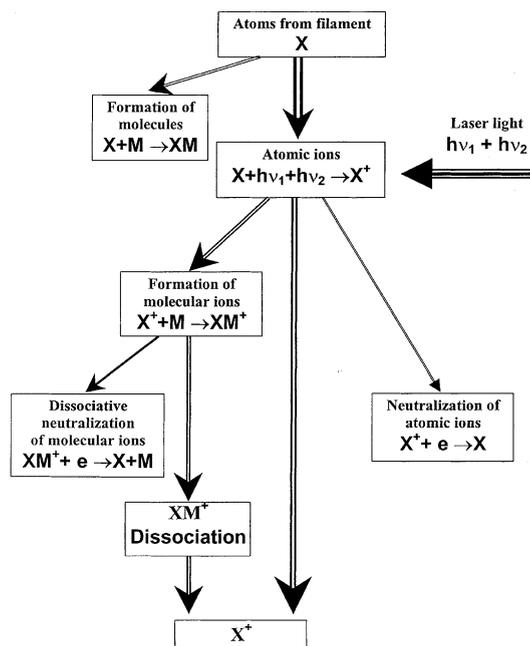
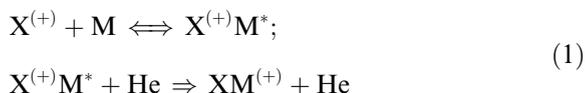


Fig. 3. The processes in the LIS at off-line conditions.

The collision complex  $X^{(+)}M^*$  is unstable with respect to dissociation but may be stabilized by a collision with a buffer gas atom. The net result can be described by a reaction rate constant  $k$  and the time evolution of the number of atoms or ions ( $n$ ) changing to molecular side bands can be described by

$$\frac{dn}{dt} = -kn[M], \quad (2)$$

with  $[M]$  the concentration of the ligand molecule. A time constant can be defined as

$$\tau = 1/k[M]. \quad (3)$$

Table 2 lists some reaction rate constants for atoms and ions. A typical rate constant for the formation of an ion–molecule adduct or a molecular

ion lies around  $k = 1 \times 10^{-10} \text{ cm}^3/\text{s}$  and with an impurity level of 1 ppm, which corresponds to the concentration  $[M]$  of  $1.35 \times 10^{13} \text{ cm}^{-3}$  at the buffer gas pressure of 500 mbar, the reaction time  $\tau$  for the formation of molecular ions  $X^{(+)}M$  becomes 740  $\mu\text{s}$ . This is a very short time in comparison to the cell evacuation time of a few hundreds ms and immediately points to the necessity for gas purification. As can be seen in Table 2, the reaction rate constants for neutral atom–molecule bonding lies roughly two orders of magnitude lower than for ions and thus the time scale will be two orders of magnitude longer.

Of particular interest and a subject of extended research is the associative reaction with water. As discussed in Section 2.4, water is the strongest impurity in helium and argon. The binding energies of some ion–water adducts, reported in Table

Table 2  
Reaction rate constants of some atoms and ions with impurity molecules

Reaction	Rate constant ( $\text{cm}^3/\text{s}$ )	Rate constant ( $\text{cm}^6/\text{s}$ )	Reference
Al + O <sub>2</sub>	$1.62 \times 10^{-10}$		[14]
	$1.79 \times 10^{-10}$		[15]
Co + O <sub>2</sub>	$1.9 \times 10^{-14}$		[16]
Cu + O <sub>2</sub>	$2.5 \times 10^{-12}$		[16]
Mo + O <sub>2</sub>	$1.2 \times 10^{-10}$		[20]
Ni + O <sub>2</sub>	$3.3 \times 10^{-11}$		[16]
Ni + DO <sub>2</sub> + CO <sub>2</sub> (10t)	$9.3 \times 10^{-13}$		[23]
Sc + O <sub>2</sub>	$5.9 \times 10^{-12}$		[18]
Ti + O <sub>2</sub>	$2.3 \times 10^{-12}$		[16]
	$1.5 \times 10^{-12}$		[17]
	$1.9 \times 10^{-12}$		[18]
	$1.6 \times 10^{-12}$		[19]
	$2.8 \times 10^{-12}$		[20]
V + O <sub>2</sub>	$4.5 \times 10^{-13}$		[18]
Mo + N <sub>2</sub>	$< 5 \times 10^{-15}$		[20]
Ti <sup>+</sup> + H <sub>2</sub> O	$6.1 \times 10^{-11}$		[13]
	$1.0 \times 10^{-10}$		[24]
Ti <sup>+</sup> (a <sup>4</sup> F) + D <sub>2</sub> O	$3.0 \times 10^{-12}$		[22]
Ti <sup>+</sup> (a <sup>2</sup> F) + D <sub>2</sub> O	$2.0 \times 10^{-10}$		[22]
Sc <sup>+</sup> + D <sub>2</sub> O	$1.3 \times 10^{-11}$		[22]
Ti <sup>+</sup> + O <sub>2</sub>	$4.55 \times 10^{-10}$		[13]
	$5.0 \times 10^{-10}$		[24]
	$5.0 \times 10^{-10}$		[21]
Th <sup>+</sup> + O <sub>2</sub>	$6.0 \times 10^{-10}$		[21]
Ti + N <sub>2</sub>	$< 5 \times 10^{-12}$		[21]
Co + O <sub>2</sub> + Ar		$1.0 \times 10^{-32}$	[16]
Ni + O <sub>2</sub> + Ar		$1.7 \times 10^{-30}$	[16]
Cu + O <sub>2</sub> + Ar		$2.0 \times 10^{-31}$	[16]

3, show that it is energetically possible to bind many water molecules.

It is also possible to form molecular ions where one or more ligands are the buffer gas atoms themselves. Table 4 gives a number of binding energies for Co and Ni ions with He, Ar.

An important neutralization reaction of the ions is the three-body reaction of the type



where helium is taken as buffer gas. The reaction depends strongly on the electron density and on the gas pressure. The three-body recombination coefficient  $\alpha$  [in  $\text{cm}^3 \text{s}^{-1}$ ], governing this reaction, is gas and pressure dependent and equals  $1.67 \times 10^{-7} \text{ cm}^3 \text{ s}^{-1}$  for the neutralization of  $\text{He}^+$  in 500 mbar He [31]. If there is a constant production of ion/electron pairs  $Q$  [in  $\text{cm}^3 \text{ s}^{-1}$ ] such as occurring when the accelerator beam passes through the gas cell, then the charge density  $n = n_{\text{ion}} = n_{\text{electron}}$  evolves in time as given [32] by the expression

$$\frac{dn}{dt} = Q - \alpha n^2, \quad (5)$$

which has as solution

$$n(t) = \sqrt{\frac{Q e^{2t/\tau} - 1}{\alpha e^{2t/\tau} + 1}}, \quad (6)$$

with a time constant  $\tau$ ,

$$\tau = (Q\alpha)^{-1/2}, \quad (7)$$

and the equilibrium density  $n_{\text{ion}} = n_{\text{electron}} = n$  is then given by

$$n = (Q/\alpha)^{1/2}. \quad (8)$$

Most of the charges created in the off-line studies are coming from the laser ionization (later we will see that the hot filament also creates a small amount of mainly potassium ions through surface ionization) and this charge creation is pulsed (pulse width is 15 ns and the repetition rate in the off-line studies is chosen such that the whole cell is evacuated before a next laser pulse is fired). Three-body recombination immediately starts after the laser pulse and the density of ions and electrons ( $n_{\text{ion}} = n_{\text{electron}} = n$ ) is governed by the following expression:

Table 3  
The binding energies of some molecules (eV)

X	$D[X^+-\text{H}_2\text{O}]^a$	$D[X(\text{H}_2\text{O})^+-\text{H}_2\text{O}]^a$	$D[X(\text{H}_2\text{O})_2^+-\text{H}_2\text{O}]^a$	$D[X(\text{H}_2\text{O})_3^+-\text{H}_2\text{O}]^a$	$D(X^+-\text{O})^b$
Co	1.70	1.68	0.67	0.59	3.29
Cu	1.67	1.77	0.59	0.55	1.62
Ni	1.90	1.74	0.70	0.53	2.78
Ti	1.64	1.41	0.69	0.86	6.93

<sup>a</sup> Ref. [25].

<sup>b</sup> Ref. [26].

Table 4  
The binding energies for some metal-noble gas ions (eV)

X	$D_0(\text{He-X})^+$	$D_0(\text{Ar-X})^+$	$D_0(\text{HeX-He})^+$	$D_0(\text{ArX-Ar})^+$
Co	0.131 <sup>a</sup>	0.508 <sup>b</sup>	0.139 <sup>a</sup>	—
Ni	0.129 <sup>a</sup>	0.55 <sup>c</sup>	0.139 <sup>a</sup>	0.513 <sup>d</sup> (calc)

<sup>a</sup> Ref. [27].

<sup>b</sup> Ref. [28].

<sup>c</sup> Ref. [29].

<sup>d</sup> Ref. [30].

$$\frac{dn}{dt} = -\alpha n^2, \quad (9)$$

which leads to a time evolution of the density

$$n = \frac{n_0}{1 + \alpha n_0 t}, \quad (10)$$

where  $n_0$  is the initial electron density. For the ions under study, the reaction coefficient  $\alpha$  is of the same order as the one for  $\text{He}^+$ . A 50% neutralization will be reached within 1 s, which is the typical evacuation time of the large cell, when the initial number of created ion/electron pairs amounts to  $\sim 6 \times 10^6 \text{ cm}^{-3}$ . This will be further discussed in Section 3.6.

In the case of molecular ions, the neutralization through dissociative recombination with electrons could be very fast as it involves only a two-body interaction of the type



The characteristic recombination time can be calculated with the equation

$$\tau = 1/\alpha[\text{e}^-], \quad (12)$$

where  $[\text{e}^-]$  is the electron density. The dissociative recombination coefficient  $\alpha$  for some molecular ions which are formed inside the ion source can reach values of  $3 \times 10^{-6} \text{ cm}^3/\text{s}$ . In this case the characteristic recombination time of 10 ms is reached at an electron concentration of  $3 \times 10^7 \text{ cm}^{-3}$ .

In order to extract information on the different processes in the gas cell, the intensity of the pure ions and of the molecular ions together with their time distribution after one laser shot will be used. It is of prime importance to understand first the flow pattern in the gas cell and at the exit hole. This will be discussed in the following section.

### 3.2. Flow pattern and ion time profile

The filament is located at a distance of 49 mm from the exit hole and 5 mm from the cell axis (see Figs. 1 and 4(a)). In the case of longitudinal ionization, the laser light ionizes atoms along the axis of the cell when they diffuse into the laser beam. At the moment  $t = 0$  (Fig. 4(b)), a cloud of atomic

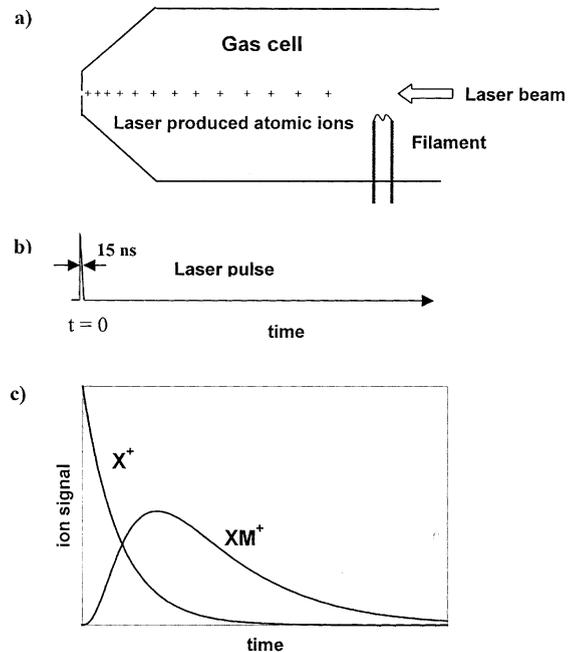


Fig. 4. The formation of the ion time profile signal after pulsed laser ionization.

ions ( $\text{X}^+$ ) is created. If the time between laser pulses is longer than the evacuation time of the cell a fresh portion of atoms is available for ionization by the next pulse. The initial ion density distribution depends on the atom distribution at the moment of ionization as the attenuation of the laser light is negligible. The laser-produced ions are evacuated with the speed of the buffer gas flow and transported through the SPIG, accelerated, mass-separated and measured in the SEM as described above. The beginning of the ion signal in Fig. 4(c) corresponds to the ions  $\text{X}^+$  created next to the exit hole; later times correspond to positions deeper inside the source. However, the observed ion time profile does not necessarily represent exactly the initial atom distribution inside the cell since some of the atoms can be in an excited state or have a chemical bonding with an impurity; furthermore the laser-produced ions can also recombine and react with impurity molecules or with the buffer gas. Fig. 4(c) is therefore only a schematic presentation of the pure ion signal and the signal of an ion in a molecular sideband.

During the development of the LIS, extensive studies have been performed on the time profiles from an off-line gas cell [33]. These profiles could recently be well reproduced in a calculation where an incompressible flow was used inside the gas cell and a quasi one-dimensional compressible flow in the region close to the exit hole [34]. For the studies presented here, the ion time profile of ions after laser ionization was calculated for the two gas cell geometries: the large cell and for the 6 mm channel cell (see Fig. 1(b)). It was assumed that the motion of atoms follows the laminar flow of the buffer gas taking into account the diffusion of atoms and ions in helium or argon buffer gas. First, the initial atom distribution was calculated assuming that all atoms originate from a point filament. The time between laser pulses was chosen to be longer than the gas cell evacuation time; therefore the atom distribution has reached its static equilibrium at the moment of laser ionization. It was also assumed that every atom was created at the filament some random time before the laser shot. Since the filament evaporation is constant in time, the distribution should be constant. At the moment of laser ionization, the time was reset and the particle's position was registered as part of the static equilibrium distribution. The calculation then continues until the particle has left the cell or struck the wall of the cell.

The result of the simulation for the large gas cell with He as buffer gas is shown in Fig. 5(a) where a radial atom distribution integrated over the angle is plotted (white points); the velocity profiles were taken from the calculations of [34]. Since the cell has a conical form, the velocity increases towards the exit hole and the atom density reduces in comparison to the density in the vicinity near the filament. Ions or atoms striking a wall were considered as lost particles. By binding the evacuation times of the points in the laser beam path (dark points), a time profile of the laser-produced ions was obtained. It is shown in Fig. 5(b) as circles. The shape of the cell, which directs the whole spatial atom distribution into the laser beam path, causes the sharp peak at time zero. For comparison, the measured nickel ion time profile (mass 58) for purified helium gas is shown in Fig. 5(b) as a solid line. The difference between exper-

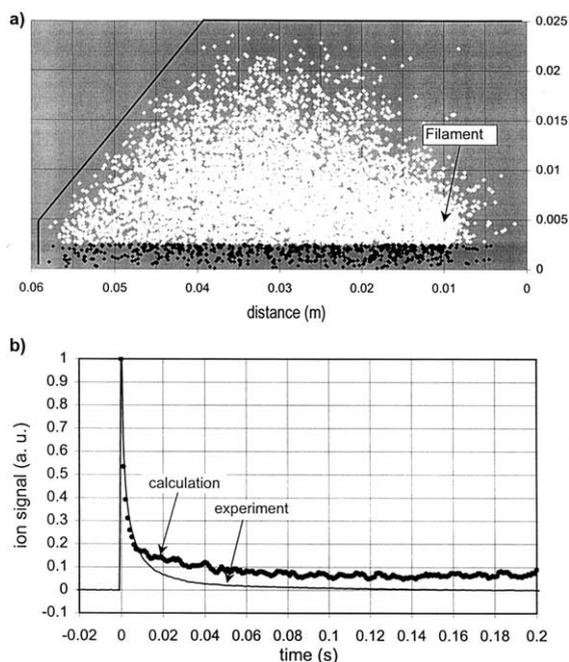


Fig. 5. (a) The radial distribution of atoms integrated over the angle evaporated from the filament in helium buffer gas of 500 mbar before the laser ionization – white points and the ions created in the laser beam path of 5 mm in diameter – black points, (b) calculated time profile of ions extracted from the gas cell shown in Fig. 1(a) – circles and experimental time profile of nickel ions at mass 58 in purified helium gas – solid line.

imental and calculated time profiles at long times ( $>10$  ms) can be explained by chemical reactions and recombination processes, which were not included in the calculation.

The ion time profile was also calculated for the channel cell. In this case the filament is located in the center of the cell and 49 mm from the exit hole. For the calculations a point source of nickel atoms was assumed. The evacuation time of the channel cell is much shorter and there is little loss of atoms and ions due to diffusion from the laser beam path. The flow is a function of the radial position and has only an axial component. The velocity distribution in the cell was extrapolated from the flow pattern calculated for the argon buffer gas [35]. The velocity profile for He was taken three times faster than for Ar, due to the difference in the exit hole conductance. Fig. 6 shows the calculated (circles) and experimental

(solid line) time profiles for Ni ions (mass 58) in argon (6a) and in helium (6b). A few observations can be made. Apart from a difference at longer times, the data obtained in argon agree with the simulations. This discrepancy at longer times which is present for the data obtained in helium as well can be due to the simple velocity profile used as well as to possible turbulences close to the filament. These are not included in the simulation and might lead to longer residence times close to the filament. The real shape of the filament was not taken into account in the calculations. This fact can be more important for He as buffer gas than for Ar because of the bigger diffusion coefficient for He. In case of the measurements in helium, the ion signal is dominated by pure Ni ions, while in the argon case molecular side bands are observed. This will be discussed further in Section 3.5. Finally, it should be noted that the amount of nickel atoms evaporated from the filament is kept low to avoid atom–electron recombination (see Section 3.6).

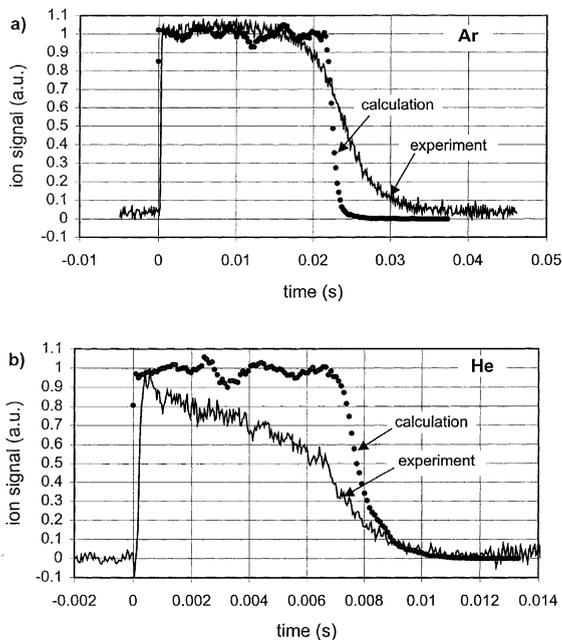


Fig. 6. Calculated (circles) and experimental (solid line) ion time profiles for argon (a) and helium (b) buffer gas from the channel cell shown in Fig. 1(b).  $P = 500$  mbar.

### 3.3. Molecular side bands and time profiles as a way to control the impurity level

The effect of the gas purification on the mass spectrum and on the ion time profile taken with the large gas cell is shown in Figs. 7 and 8. Fig. 7(a) presents the mass spectrum of the laser ionized nickel atoms in helium if the gas is not purified. The main impurity in the helium gas comes from moisture at the level of 390 ppb. The strongest peak is  $\text{Ni}(\text{H}_2\text{O})_3^+$  ( $M = 112$ ). If the helium gas is flowing through the gas purifier, the relative intensities of the atomic nickel ions and the intensity of the ions in the molecular side bands does change dramatically, see Fig. 7(b). The peak at mass 112 is reduced almost to zero and the

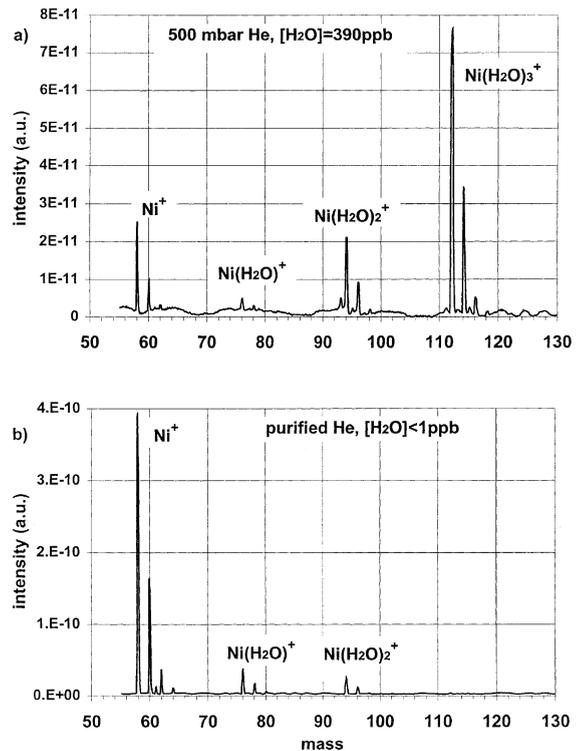


Fig. 7. (a) The mass spectrum of ions extracted from the gas cell after laser ionization of nickel atoms in non-purified helium. Nickel has five stable isotopes,  $M = 58, 60, 61, 62$  and  $64$  with relative abundance of 68.27%, 26.10%, 1.13%, 3.59%, 0.91%, respectively. The concentration of impurities in a gas cylinder measured at the factory: moisture – 390 ppb;  $\text{N}_2, \text{O}_2, < 20$  ppb; (b) the same as in (a) but helium gas passed the gas purifier.

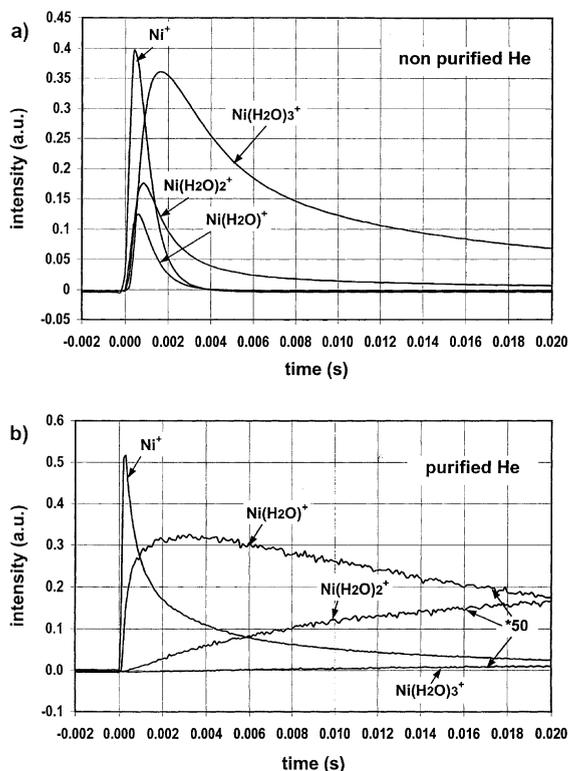
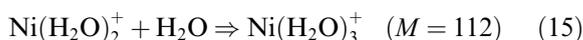
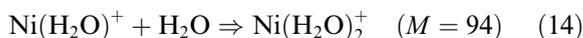
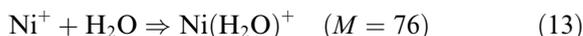


Fig. 8. The time profiles of ions extracted from the gas cell after laser ionization of nickel atoms at mass 58-Ni, 76-Ni<sup>+</sup>(H<sub>2</sub>O), 94-Ni<sup>+</sup>(H<sub>2</sub>O)<sub>2</sub>, 112-Ni<sup>+</sup>(H<sub>2</sub>O)<sub>3</sub>. (a) Non-purified helium with moisture concentration of 390 ppb, (b) helium gas is purified to the sub ppb level. The vertical scale for the Ni<sup>+</sup>(H<sub>2</sub>O), Ni<sup>+</sup>(H<sub>2</sub>O)<sub>2</sub> and Ni<sup>+</sup>(H<sub>2</sub>O)<sub>3</sub> ions is increased by a factor 50.

strongest ion signal is now at mass 58 (<sup>58</sup>Ni<sup>+</sup>). These strong differences are also observed in the ion time profile signals. Fig. 8(a) shows the ion signals of nickel and nickel hydrate ions created in the non-purified helium with moisture concentration of 390 ppb. The time behavior indicates that the following sequence of hydration occurs:



The buffer gas atom, needed for stabilizing the collision, is not included in Eqs. (13)–(15). The

time difference between the production maxima of the different hydrates lies in the ms region, which indicates that indeed the estimation of the reaction rate constants used in Eq. (2) is in the right order. The effect of the gas purification is clearly seen from Fig. 8(b). Due to the decreased concentration, the reaction time is much longer and thus the total intensity of the molecular ion signals is much smaller. Note that the plotted ion signals for the Ni<sup>+</sup>(H<sub>2</sub>O), Ni<sup>+</sup>(H<sub>2</sub>O)<sub>2</sub> and Ni<sup>+</sup>(H<sub>2</sub>O)<sub>3</sub> ions are increased by a factor 50. These mass spectra give us a good handle on the level of impurities in the gas cell.

### 3.4. Ion–impurity interactions

The influence of impurities in the buffer gas can best be studied by adding a known amount of these molecules to the purified buffer gas. Unfortunately it was not possible to admix in a controlled way a specific amount of water, therefore our studies have been limited to N<sub>2</sub> and O<sub>2</sub> as impurities. Table 3 shows the binding energies of some metal ions with water molecules forming hydrates and with oxygen forming oxides. To study the dependence on the type of ion we used ions from Ni, Co and Ti.

#### 3.4.1. Ni + N<sub>2</sub>

Fig. 9 shows mass spectra of ions produced in the large gas cell for pure helium ([N<sub>2</sub>] < 1 ppb) (Fig. 9(a)) and helium with a concentration of nitrogen gas of 0.5 ppm (Fig. 9(b)) and of 5 ppm (Fig. 9(c)). When 0.5 ppm nitrogen is added to the pure helium, the Ni<sup>+</sup> peak decreases with a factor of 4 and new molecular ions such as NiN<sub>2</sub><sup>+</sup>, NiN<sub>2</sub>(H<sub>2</sub>O)<sup>+</sup> and Ni(N<sub>2</sub>)<sub>2</sub><sup>+</sup> are appearing together with an increase of the intensities of the nickel hydrates. In fact adding 0.5 ppm nitrogen means also adding 0.045 ppb of H<sub>2</sub>O and this rises the intensity of the Ni(H<sub>2</sub>O)<sup>+</sup> peak by a factor 4. Increasing the nitrogen concentration up to 5 ppm causes further reduction of the Ni<sup>+</sup> peak and changes the intensities of the molecular side bands. The ion time profiles, which are shown in Fig. 10 at concentrations 0.5 and 5 ppm and

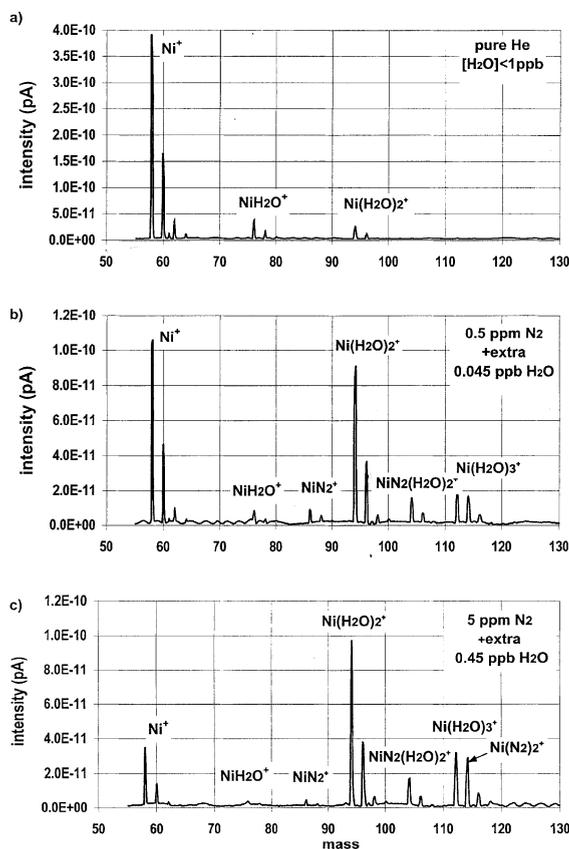


Fig. 9. The influence of nitrogen admixture in purified helium on mass spectrum of ions extracted from the large gas cell after laser ionization of nickel atoms: (a) the pure helium, (b) the nitrogen concentration – 0.5 ppm, (c) the nitrogen concentration – 5 ppm. The vertical scale can be used to compare the signal intensities.

which can be compared with the time profiles in Fig. 8 for the pure and unpurified helium case, show that a complex network of chemical reactions does take place inside the gas cell. For the two concentrations of  $N_2$  admixtures, the formation of molecular ions start with  $NiN_2^+$  and  $Ni(H_2O)^+$ , see Fig. 10. Although the moisture concentration is about  $10^4$  times smaller compared to the  $N_2$  concentration, the slope of the bonding reaction with  $H_2O$  is only four times smaller than the one for  $N_2$  (Fig. 10(a)). Thus the reaction rate constant ( $k_{H_2O}$ ) is about 2500 times higher compared to  $k_{N_2}$ . Out of the sequence of the successive reactions at longer time scales, one

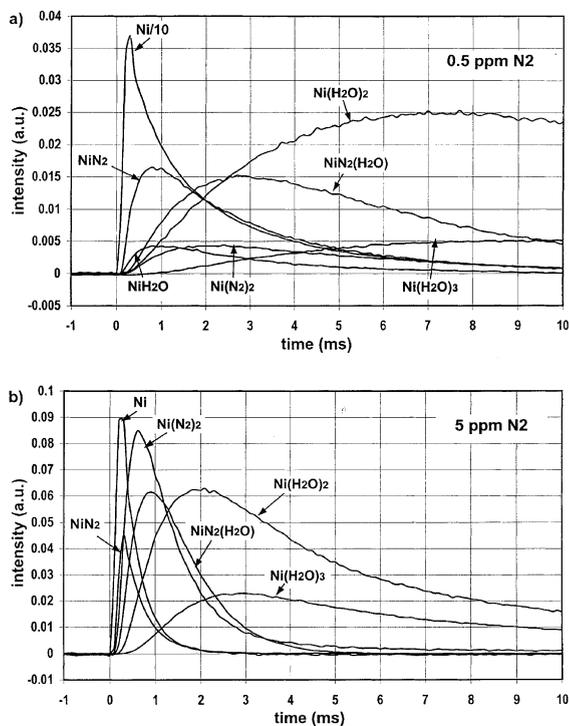


Fig. 10. The time profiles of ions extracted from the large gas cell at different concentration of nitrogen in the purified helium gas: (a) 0.5 ppm, (b) 5 ppm. The vertical scale in (a) for nickel ions is reduced by a factor 10. Although the vertical scales are given in arbitrary units, the scales from (a) and (b) can be compared.

can conclude that the presence of nitrogen has a catalytic effect in forming finally  $Ni(H_2O)_2^+$  and  $Ni(H_2O)_3^+$ . A last observable is the total intensity: it drops with a factor of 1.8 when adding 0.5 ppm  $N_2$  to the purified helium and with a factor of 1.2 when going from 0.5 to 5 ppm  $N_2$ . The loss of ions when increasing the nitrogen concentration can be due to two reasons. First, the concentration of nickel atoms in their atomic ground state near the exit hole region can be reduced because of the reaction of nickel atoms with nitrogen. The second reason could be that the fast reactions of nickel ions with nitrogen and water molecules lead to molecular ions that are more easily neutralized. The relative importance of both mechanisms cannot be deduced from these measurements.

### 3.4.2. Ni + O<sub>2</sub>

The influence of admixing oxygen with the helium gas on the mass spectrum of ions extracted from the gas cell after laser ionization of nickel atoms is shown in Fig. 11. The amplitudes of the peaks can directly be compared since no changes were made except adding oxygen gas. Already at a concentration of 0.5 ppm, the nickel ion reduces 35 times and at 5 ppm it disappears in the background. The oxygen has a stronger influence on the nickel ion signal than nitrogen. The ion profiles at the oxygen admixture of 0.5 ppm are shown in

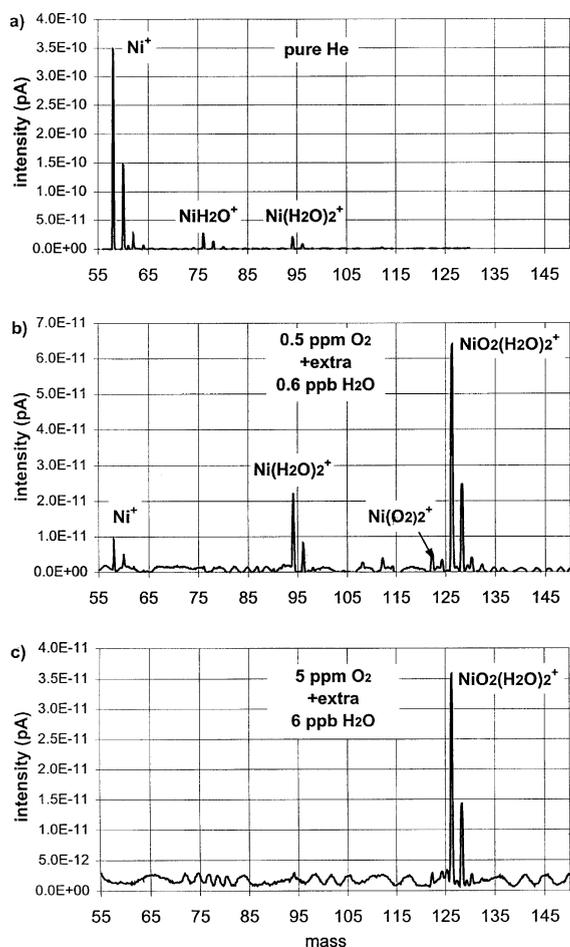


Fig. 11. The influence of oxygen admixture in purified helium on the mass spectrum of ions extracted from the large gas cell after laser ionization of nickel atoms: (a) the pure helium, (b) the oxygen concentration – 0.5 ppm, (c) the oxygen concentration – 5 ppm.

Figs. 12(a) and (b). Again as in the case of nitrogen, the first molecular ions formed are NiO<sub>2</sub><sup>+</sup> and Ni(H<sub>2</sub>O)<sup>+</sup>. The added concentration of water through its presence in the He + O<sub>2</sub> mixture is 0.6 ppb which is a factor of 1000 less compared to the O<sub>2</sub> impurity concentration. As the slope for the formation of NiO<sub>2</sub> and NiH<sub>2</sub>O is similar (see Fig. 12(a)), the reaction rate constant  $k_{\text{H}_2\text{O}}$  is about 1000 times larger than  $k_{\text{O}_2}$ . Taking into account the comparison of the reaction rate constant of water and N<sub>2</sub> it means that  $k_{\text{O}_2}$  is a factor 2.5 times larger than  $k_{\text{N}_2}$ . The time sequence of the different chem-

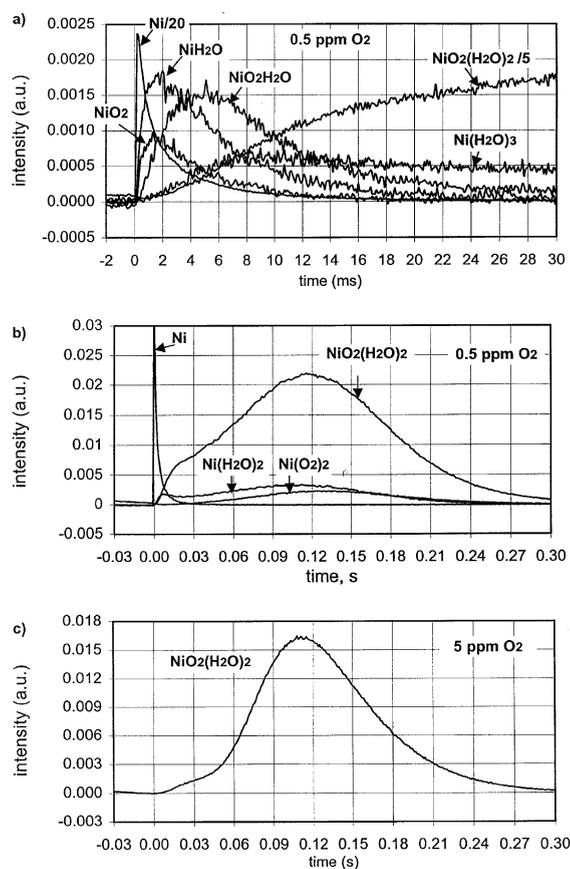


Fig. 12. The time profiles of ions extracted from the large gas cell at different concentrations of oxygen in the purified helium gas: (a) and (b) 0.5 ppm, (c) 5 ppm. Although the vertical scales are given in arbitrary units they can be used to compare the amplitude of the signals in (a), (b) and (c). The vertical scale in (a) is reduced by a factor 20 for nickel ions and by a factor 5 for NiO<sub>2</sub>(H<sub>2</sub>O)<sub>2</sub>.

ical reactions is quite complicated but does end in the formation of  $\text{Ni}(\text{H}_2\text{O})_2^+$ ,  $\text{Ni}(\text{O}_2)_2^+$  and  $\text{Ni}(\text{O}_2)(\text{H}_2\text{O})_2^+$ . Adding 5 ppm of  $\text{O}_2$  leads to a very peculiar time profile (see Fig. 12(c)) where most of the intensity is concentrated in the  $\text{Ni}(\text{O}_2)(\text{H}_2\text{O})^+$  peak. The absence of any ion signal in the beginning of Fig. 12(c) indicates that no atomic Ni survives the transport to the exit hole and that all Ni atoms are most probably converted to an oxide.

### 3.4.3. Ti + H<sub>2</sub>O, Ti + O<sub>2</sub>

Although at first sight the IGISOL technique does not show a strong dependence on the chemical properties of the radioactive ions of interest [1], it is clear that the reaction rate constants are changing from one element to the other and there could be substantial differences. To illustrate this further we discuss the example of Ti ions. Titanium is an element of particular nuclear physics interest and considerable efforts were devoted at the LISOL set up to the production of laser-ionized neutron-deficient Ti isotopes. Surprisingly the total efficiency for laser ionization of Ti was rather low. Therefore the behavior of laser-ionized Ti ions was studied in a series of off-line experiments. Fig. 13(a) shows a mass spectrum of the ions created inside the gas cell after laser ionization of titanium atoms in purified helium. A comparison with Fig. 7(b) shows that the  $\text{Ti}^+$  ions react more efficiently with the residual impurities (mostly water) than the  $\text{Ni}^+$  ions. Furthermore a number of side bands in the Ti spectrum are based on the TiO molecule. The formation of the TiO ions is probably not mostly due to the presence of oxygen but rather to the presence of water molecules. It is known that  $\text{Ti}^+$  is very active towards breaking C–H, N–H and C–O bonds and the H–O bond in water molecules. All these reactions are exothermic at thermal energies. The titanium ions display a very strong bond to oxygen atoms [24,36]. The next scheme shows a mechanism of dehydrogenation of H<sub>2</sub>O by  $\text{Ti}^+$  proposed in [37],

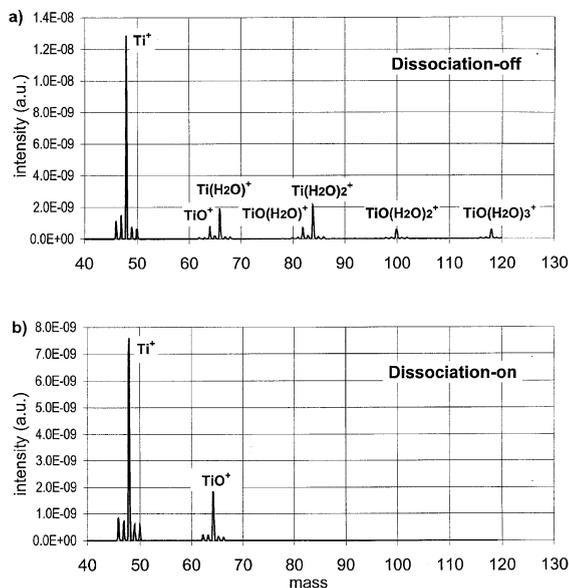
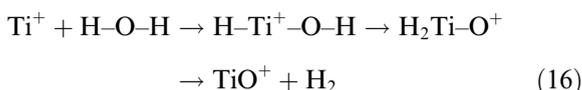


Fig. 13. The mass spectrum of ions extracted from the large gas cell after laser ionization of titanium atoms in purified helium. (a) No dissociation voltage between the gas cell and the SPIG is applied, (b) dissociation voltage of 250 V is applied to dissociate molecular ions coming out the gas cell. There are five stable titanium isotopes  $^{46-50}\text{Ti}$  with natural abundance of 8%, 7.3%, 73.8%, 5.5% and 5.4%, respectively.

A detailed discussion of all possible elimination mechanisms of H<sub>2</sub> can be found in [38]. The  $\text{TiO}^+$  ion is the only exothermic reaction product. The above-mentioned results have been obtained in a drift tube reactor with 1 Torr of He as a buffer gas. In the LIS a much higher buffer gas pressure is used. In this condition two primary exothermic reaction products are observed. These are  $\text{TiO}^+$  and  $\text{TiH}_2\text{O}^+$ . The time profiles of these molecular ions are identical, see Fig. 14(a). This means that both ions have an identical history inside the cell, which is defined by the reaction of Ti ions with water molecules. This fact can be explained by the formation of the excited ion–molecule complex  $\text{TiH}_2\text{O}^{+*}$  which decays later on through the two channels: the first one with formation of  $\text{TiO}^+$  ions and the second one with formation of non-excited  $\text{TiH}_2\text{O}^+$  ions which are stabilized via collisions with helium atoms. The profiles were measured on the masses 64 and 66 for  $\text{TiO}^+$  and  $\text{TiH}_2\text{O}^+$ , respectively. The contribution of the  $^{46}\text{TiH}_2\text{O}^+$  ions into the  $^{48}\text{TiO}^+$  signal and the contribution of the

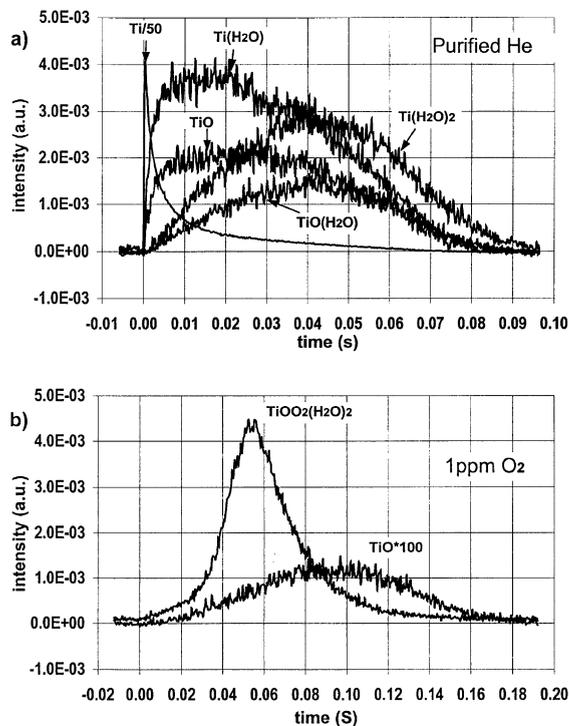


Fig. 14. The time profiles of ions extracted from the large gas cell after laser ionization of titanium atoms at different concentration of oxygen in helium gas: (a) the purified helium, the vertical scale for  $\text{Ti}^+$  is reduced by a factor 50; (b) the oxygen concentration  $\sim 1$  ppm; the vertical scale for  $\text{TiO}^+$  is increased by a factor 100.

$^{50}\text{TiO}^+$  ions into the  $^{48}\text{TiH}_2\text{O}_2^+$  signal are small due to the low abundances of  $^{48}\text{Ti}$  (8%) and  $^{50}\text{Ti}$  (5.4%) relative to  $^{46}\text{Ti}$  (73.8%). Figs. 14(b) and 15(a) illustrate how sensitive the titanium atoms are to the presence of oxygen molecules in the purified helium gas. At a 1 ppm concentration of oxygen only one peak remains, namely at mass 132. This peak can be identified as consisting of  $\text{TiO}(\text{O}_2)(\text{H}_2\text{O})_2^+$  ions. The amount of titanium atoms available for the ionization in the exit hole region is essentially reduced to zero due to a reaction with oxygen. The reaction time of titanium atoms with oxygen molecules at a concentration of 1 ppm can be estimated from the reaction rate constant of  $2 \times 10^{-12} \text{ cm}^3/\text{s}$  (an average value in Table 2). This time equals  $\sim 25$  ms which is much smaller than the travel time of titanium atoms from the filament to the exit hole, 0.5 s. A similar conclu-

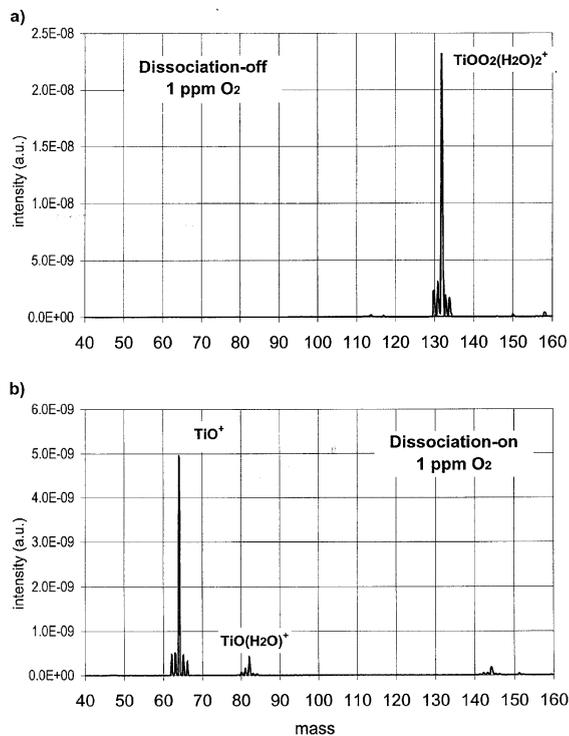


Fig. 15. The mass spectrum of ions extracted from the large gas cell after laser ionization of titanium atoms in helium gas with the oxygen concentration of 1 ppm: (a) without dissociation voltage, (b) with a dissociation voltage of 250 V.

sion was made for nickel atoms in the presence of oxygen.

### 3.5. Ion–buffer gas interactions

The choice of the buffer gas for storing and transporting the radioactive ions after their production in a nuclear reaction depends on a number of parameters. The stopping power defines the efficiency for slowing down the products recoiling out of the target; the survival of the thermalized ions will strongly depend on the ionization potential of the buffer gas. Also flow and diffusion is dependent on the kind of buffer gas. Another important characteristic is that ions not only form stable bonds with impurities present at the ppb level in the buffer gas but also with the buffer gas atoms themselves. This effect is present in helium as buffer gas but is most clearly observed with

argon and could have further consequences on the time scale of the different recombination reactions and thus on the efficiency of the gas cell.

Figs. 16(a) and (b) show the mass spectrum of ions coming out of the large gas cell after laser ionization of cobalt atoms in respectively purified argon and purified helium. For these studies cobalt atoms were taken for laser ionization, as cobalt is a mono-isotopic element making the identification of the different mass peaks more straightforward. In argon not only cobalt hydrates are present but also cobalt–argon-based molecular ions with similar intensities. Also in helium, cobalt–helium-based molecular ions are present but their relative importance is much smaller (note the logarithmic scale in Fig. 16(b)). Table 4 shows the binding

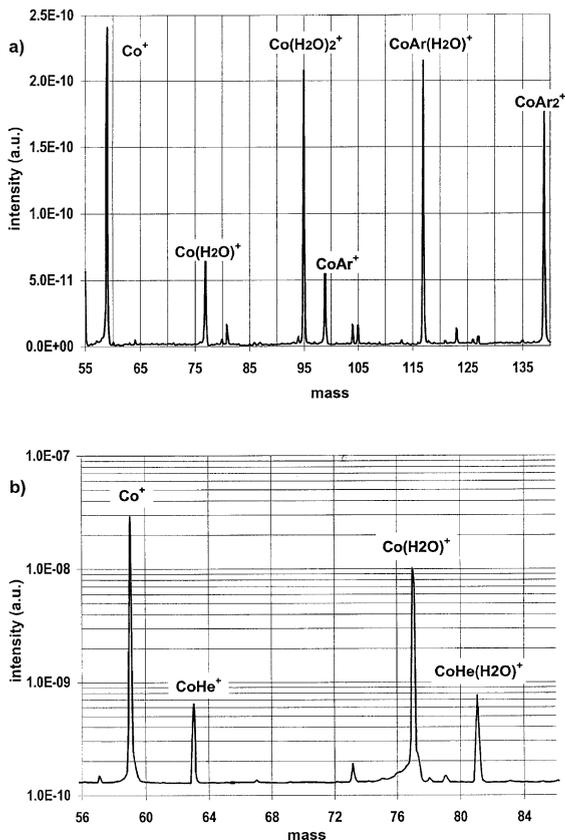


Fig. 16. (a) The mass spectrum of ions from the LIS after laser ionization of Co atoms in 500 mbar of purified Ar. Cobalt has only one isotope. (b) Mass spectrum of ions from the LIS after ionization of cobalt atoms in 500 mbar of He.

energy of cobalt and nickel ions with argon and helium. The binding energy of ions with helium is much smaller than with argon, which could explain the low intensity of the  $\text{CoHe}^+$  and  $\text{CoHeH}_2\text{O}^+$  ions. Time information about the formation of molecular ions of nickel in purified argon is shown in Fig. 17 for the channel cell. A low temperature of the nickel filament was used in this measurement to exclude recombination processes (see next section). The strongest signal comes from the atomic  $\text{Ni}^+$  ions and does show the typical time profile of the channel cell (see Section 3.2). The  $\text{NiAr}_n^+$  ( $n = 1-3$ ) molecular ions are formed extremely fast and especially  $\text{NiAr}_2^+$  is formed efficiently but this particular molecular ion does not survive long as conversion to  $\text{NiArH}_2\text{O}^+$  and  $\text{Ni}(\text{H}_2\text{O})_2^+$  does take place. Note that the sum of the time profile of the  $\text{NiAr}^+$ ,  $\text{NiAr}_2^+$ ,  $\text{NiAr}_3^+$ ,  $\text{NiArH}_2\text{O}^+$ ,  $\text{Ni}(\text{H}_2\text{O})$  and  $\text{Ni}(\text{H}_2\text{O})_2$  ions show the same behavior as the  $\text{Ni}^+$  ions. This indicates that the molecular ions mentioned above as well as the Ni ions have an ion-survival probability that is large compared to the evacuation time scale which is about 20 ms. The process that makes the initial  $\text{Ni}/\text{NiAr}/\text{NiAr}_2/\text{NiAr}_3$  distribution at very short time scale ( $< 50 \mu\text{s}$ ) is not understood. Because of the extremely short time scale and because all ions are created via photo-ionized Ni, this process must be induced by a catalytic process that stops after  $< 50 \mu\text{s}$ . The origin of this process is not known.

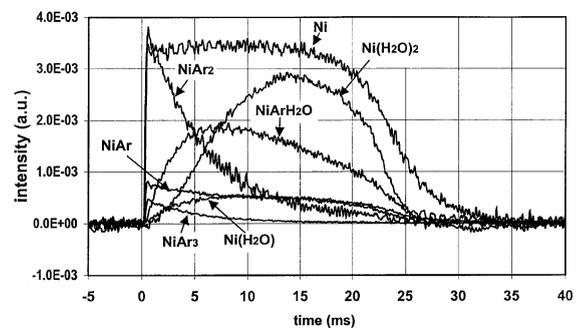


Fig. 17. The time profiles of ions extracted from the channel gas cell after laser ionization of nickel atoms in 500 mbar of purified Ar. The filament temperature is low enough to exclude recombination of ions.

### 3.6. Ion survival as a function of the ion/electron density

Neutralization of laser-produced ions through three-body ion–electron recombination (see Eq. (4)) can change the time profile of the ions extracted from the gas cell. In principle, the time scale of the recombination process is given by Eq. (5), however in the case of laser ionization, the creation of ions is finished after 15 ns. The recombination term in the Eq. (5) is six orders of magnitude smaller than the production term  $Q$  at the maximum ion density used in the experiments. In this case the equilibrium ion–electron density (8) created by the laser pulse is simply defined by the amount of atoms available for ionization. This density can be varied by changing the Ni filament temperature. To minimize the problems in understanding the time profiles, we used the channel gas cell where a rather flat evacuation profile is expected as discussed in Section 3.2. Furthermore the ion/electron pair creation by the laser pulse is restricted to the laser interaction zone which has a cross section of  $\sim 12 \text{ mm}^2$ . The effects of diffusion of atoms and ions in and out of the laser beam path and diffusion losses to the wall are considered as minimal in the channel gas cell. Fig. 18(a) shows the time profiles of nickel ions in helium at different filament temperatures. The filament temperature decreases when going from profile 5 to 1 and this leads to a drop in ion current for 5 pA at  $T_5$  to 30 fA at  $T_3$  and to 0.6 fA at  $T_1$ . The ion current was measured in a Faraday cup at  $T_5$  and  $T_4$  at a laser pulse repetition rate of 20 Hz. The values at lower temperatures  $T_3 - T_1$  were deduced from the ion time profiles. In order to compare the profiles, all maximums have been normalized to 1 (at  $t = 0 \text{ ms}$ , the time of the laser pulse). The ion concentration can be estimated from the total current extracted from the gas cell before mass separation assuming a transport efficiency through the SPIG of 50%. The atomic  $\text{Ni}^+$  ions are responsible for more than 90% of the laser-produced ions. At the maximum temperature  $T_5$ , the ion concentration is  $\sim 1 \times 10^7 \text{ ions/cm}^3$ . It decreases over  $4 \times 10^4 \text{ ions/cm}^3$  for  $T_3$  to  $1 \times 10^3 \text{ ions/cm}^3$  for  $T_1$ . The curves  $T_3$ ,  $T_2$  and  $T_1$  are quite similar which indicates that at this level of ion/electron density there is little recom-

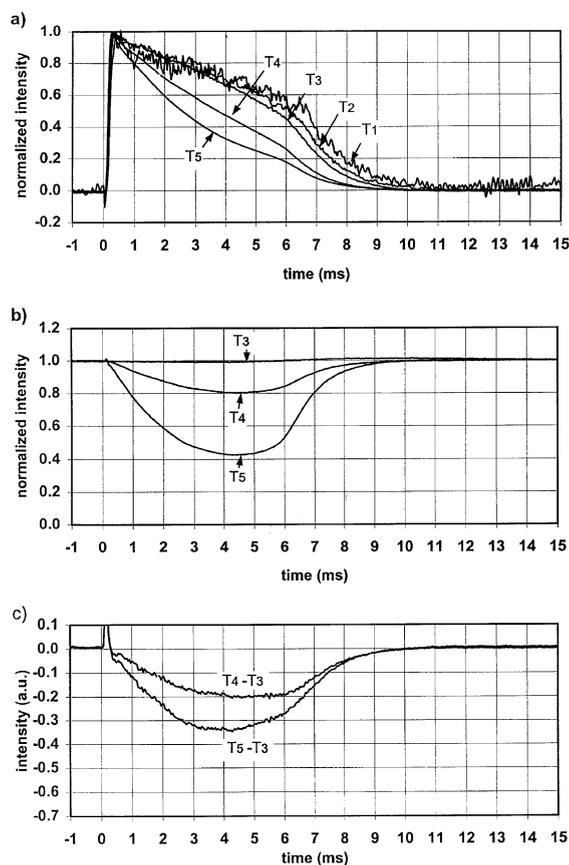


Fig. 18. (a) Normalized time profiles of laser-produced nickel ions in helium buffer gas (500 mbar) at mass 58 and at different filament temperatures  $T_5 > T_4 \dots > T_1$  from the channel gas cell; (b) normalized current of potassium ions at mass 39 at different temperatures of the nickel filament  $T_5 > T_4 > T_3$ ; (c) the difference between two normalized nickel ion signals,  $T_4 - T_3$  and  $T_5 - T_3$ .

bination within the 7 ms time scale of the cell evacuation. The curves  $T_4$  and  $T_5$  are strongly deviating from curve  $T_1$  showing loss of ions due to ion/electron recombination. The simulation of the time evolution according to (10) at different temperatures shows a good agreement with experimental behavior during the first 3 ms, however the recombination coefficient was not extracted since a detailed analysis of electron loss is required. This effect of neutralization through ion/electron recombination can also be seen in the ion signal at mass 39 due to  $\text{K}^+$  ions. Potassium, present as impurity in the nickel filament, is constantly

evaporated and partly surface-ionized. Fig. 18(b) shows the influence of the laser ionization of nickel on the potassium current at three different nickel filament temperatures. At temperature  $T_3$  (corresponding with an ion concentration is  $\sim 4 \times 10^4$  ions/cm<sup>3</sup>), no effect is seen on the constant  $K^+$  current, (here normalized to 1) by the laser pulse which starts at  $t = 0$  laser pulse. At higher filament temperatures, the DC potassium current is temporally reduced due to recombination with electrons produced during the laser ionization of nickel atoms. This neutralization increases until it reaches a plateau from 3 to 5 ms; then it decreases again as the laser-produced ions and electrons are evacuated. When subtracting the normalized  $T_5$  and  $T_4$  curves from the  $T_3$  curve in Fig. 18(a) one obtains the curves in Fig. 18(c). They have a similar shape as the curves of Fig. 18(b), which indicates that the three-body electron-ion-helium recombination coefficients for nickel and potassium ions are of the same order of magnitude.

### 3.7. Dissociation of molecular ions in the acceleration voltage of the SPIG

Applying a voltage between the gas cell and the RF ion guide can decompose most of molecular ions, which are formed inside the gas cell. Fig. 19 shows the mass spectrum of cobalt ions that are detected in a non-purified (grade – 6.0) helium gas without and with a dissociation voltage of 250 V. All molecular ions, which are formed in the reactions with impurity molecules are destroyed and up to 80% of them are converted into the atomic ion  $Co^+$  peak. The small  $Co_2^+$  peak appears as a result of dissociation of molecular ions, which are formed in the filament region where the concentration of cobalt atoms is high. At low dissociation voltage ( $\sim 30$  V), first the  $Co(H_2O)_3^+$  peak decreases but the  $Co(H_2O)_2^+$  peak grows. This means that the heavy molecular ions are converted into the lighter ones. At higher voltage the  $Co(H_2O)_2^+$  ions are converted in the  $Co(H_2O)^+$  ions, etc. We observe the decomposition of all molecular ions, which nickel, cobalt, rhodium and copper atomic ions form in reactions with  $O_2$ ,  $N_2$ ,  $H_2O$ , He and Ar. Only titanium ions behave differently. As was

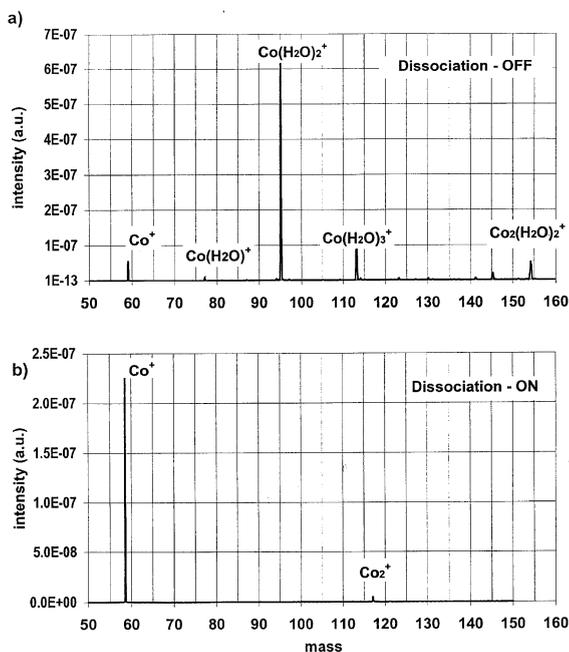


Fig. 19. Dissociation of molecular ions in the acceleration electrical field between the gas cell and the RF ion guide. The mass spectrum of ions from the gas cell after laser ionization of cobalt atoms in non-purified helium (grade-6.0) at 500 mbar without (a) and with (b) electrical field (250 V).

already shown in Fig. 13(a), the titanium ions break the water molecules and form  $TiO$  ions. If the dissociation voltage of 250 V is applied, all molecular ions, which are formed from the primary  $Ti(H_2O)_n^+$  ions are converted in  $Ti^+$  ions. All the  $TiO(H_2O)_n^+$  molecular ions are converted into the  $TiO^+$  ions, see Fig. 13(b). The  $TiO^+$  ions cannot be dissociated with the maximum dissociation voltage of 300 V. This effect can be explained by the very large binding energy of 6.93 eV for  $TiO^+$  [26]. The binding energies of  $(Ti^+-H_2O)$  and  $(TiH_2O^+-H_2O)$  are much smaller, see Table 3. The amount of energy that ions can gain while being accelerated in an electrical field in helium gas has been calculated for Ar ions in helium by a Monte-Carlo method using the  $Ar^+-He$  interaction potential. Fig. 20 shows the maximum energy of  $Ar^+$  ions in electrical field of 100 and 1000 V/cm as a function of a buffer gas pressure. The pressure drop when going from the buffer gas cell to the vacuum chamber containing the SPIG was from

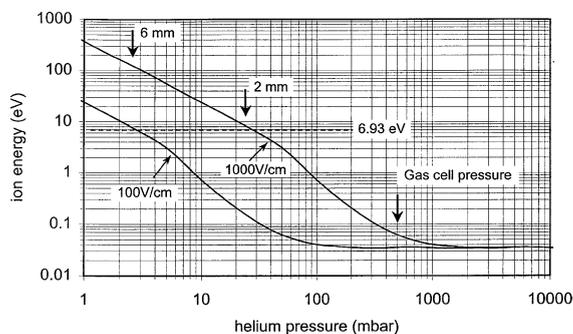


Fig. 20. The mean energy of  $\text{Ar}^+$  ions gained in electrical fields of 100 and 1000 V/cm as a function of the helium gas pressure. It is assumed that the time that ions spent in the field is not limited. The arrows indicate the gas pressure in the cell, after 2 mm of expansion and after 6 mm of expansion. Also indicated is the energy needed to break up TiO molecules.

500 mbar to  $2 \times 10^{-2}$  mbar but in the acceleration zone of the helium jet expansion implies a roughly quadratic decrease in function of the distance from the exit hole [39]. The distance between the SPIG rods and the exit hole can be varied from 2 to 6 mm (estimated pressure respectively 22 mbar and 2.4 mbar, see arrows in Fig. 20) and the voltage between 0 and 300 V. The actual energy gain depends not only strongly on the pressure and field strength (see Fig. 20) but also on the time spent in particular pressure-field configuration as the final energy is only gained after considerable number of collisions. In the configuration when the rods are at 2 mm, we can accelerate ions enough to dissociate them (except TiO) and *the subsequent collisions after the dissociation can cool down the gained back to gas temperature energies*. The ion cooling capacity of the SPIG is discussed in [6]. The results of detailed experiments, calculations and simulations will be presented in a forthcoming paper [40].

#### 4. Electrical fields inside the cell

Electrical fields inside the gas cell could influence the fate of the ions in a dramatic way. Focusing fields could drag the ions faster out of the cell and could also prevent the ions from diffusing to the walls where they would be lost. Furthermore the more mobile electrons could be fastly removed

thereby diminishing ion losses from ion–electron neutralization reactions. Another benefit could be the breaking up of molecular ions but unfortunately, by inspecting Fig. 20, the energy gain in the electrical field of 1000 V/cm is limited in the high-pressure region (above 500 mbar) to less than 60 meV which is lower than most binding energies (see Tables 3 and 4). Our first aim to apply electrical fields inside the gas cell was to improve the selectivity of the LIS.

The selectivity in on-line conditions is defined as the ratio of the ion current of the studied element with lasers tuned in resonance to the ion current with lasers set off resonance. The obtained selectivity in the on-line experiments reaches a few hundreds for light ion-induced fusion–evaporation reactions [3] and is determined by the survival probability of nuclear reaction products in ionic form after thermalization in the noble gas. The small fraction of ions that arrives at the exit hole could eventually be further reduced by applying an electrical field inside the gas cell [5,41]. To study such a possibility, two grids separated by 2.5 mm with a transmission of more than 95% were installed inside the gas cell as shown in the inset of Fig. 21. The distance between the exit hole and the first grounded grid equals 7 mm. A DC or pulsed voltage  $V_{\text{grid}}$  can be applied to the second grid located at a distance of 2.5 mm from the grounded one. The idea of this setup for on-line conditions is to suppress the evacuation of non-neutralized ions and to use the transverse beam path for laser ionization. This configuration was tested in off-line experiments. Ni ions were produced by longitudinal laser ionization of nickel atoms along the axis of the cell at 500 mbar of He. No dissociation voltage was applied between the ion source and the SPIG. Fig. 21 shows the time profiles of nickel ions at mass 58 at zero potentials of the grid  $V_{\text{grid}} = 0$  as well as positive or negative potential of the grid. The evacuation time of ions created on the axis of the cell at the distance of 7 and 9.5 mm equals 5 and 12 ms, respectively. As can be seen from Fig. 21, in contrast to the situation when 0 voltage is applied no ions are observed after more than 5 ms if  $V_{\text{grid}} > +30$  V or  $V_{\text{grid}} > -100$  V. Furthermore the positive voltage pushes the ions towards the exit hole. At small positive voltages (up to +3 V) a

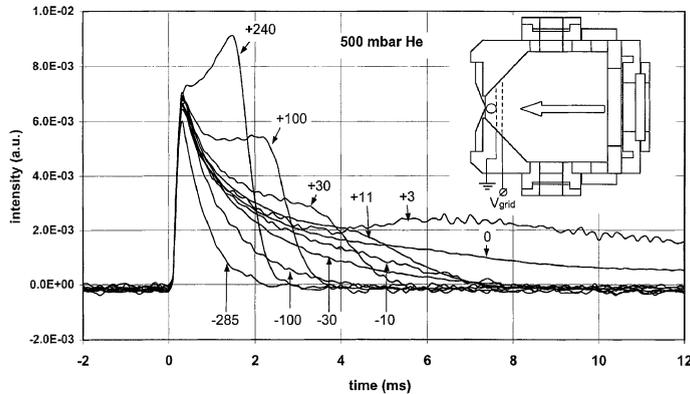


Fig. 21. The time profile of nickel ions extracted from the ion source after longitudinal laser ionization at different potentials applied to the grid  $V_{\text{grid}}$ .  $P_{\text{He}} = 500$  mbar. The inset shows the large gas cell with two grids located at the distance of 7 and 9.5 mm from the exit hole.

bigger signal is observed from the region between the grids. This enhancement can be explained by the effective removal of electrons in the laser ionization zone thus reducing the ion–electron neutralization process. The positive electrical field is not yet large enough to influence the ions. So, in principle it is possible to use electrical fields inside the gas cell and it is possible to collect all ions between the two grids even with a 240 V electrical pulse of 2 ms. But in on-line conditions the plasma created by the impinging beam and high radioactivity reduces the effect of electrical fields severely. This will further be discussed in the next paper.

## 5. Ion source efficiency

In order to obtain a quantitative measure of the total off-line efficiency a known amount of radioactive atoms of  $^{57}\text{Co}$  ( $T_{1/2} = 272$  d) was brought into the buffer gas, photo-ionized and mass-separated. The ratio of the time-integrated beam intensity of  $^{57}\text{Co}$  ions and the total number of isotopes fed into the buffer gas determined the efficiency.

The radioactive cobalt isotopes were deposited on previously annealed molybdenum filaments leading to typical source strengths of  $1 \mu\text{Ci}$ . Part of the  $^{57}\text{Co}$  atoms was evaporated in the gas cell by heating the filament. The radioactivity of the filament before and after heating was measured via

the detection of the 122 keV  $\gamma$ -ray of  $^{57}\text{Co}$  using a Ge detector. In one heating cycle, typical values for the amount of activity that was evaporated from the filament varied between 10% and 50%. The  $^{57}\text{Co}$  atoms evaporated from the filament were subsequently ionized by the laser light, extracted from the gas cell and mass separated. The pulse repetition rate of the lasers was increased to 200 Hz. In order to verify the laser frequency and to optimize the mass separator settings, a cobalt filament was installed to produce a cloud of stable cobalt atoms. This optimization procedure was performed prior to the evaporation of the  $^{57}\text{Co}$ . After mass separation the mass 57 ion beam was implanted into an aluminium foil. The total efficiency of the ion source was obtained by comparing the activity present on the aluminium foil with the activity evaporated from the molybdenum filament. Measurements were performed using the larger gas cell with purified helium as well as purified argon as buffer gas, a pressure of 500 mbar was used in both cases. Furthermore the filament could be placed at two different positions: at 15 and at 49 mm from the exit hole. The overall efficiency in helium was 7.9% and 1.8%, respectively. This difference in efficiency points to an important loss of cobalt atoms in their atomic form when they linger for a longer time inside the gas cell. The loss of photo-ions due to recombination can be neglected because of the very low concentration of the cobalt atoms in the ionization volume due to

slow evaporation of radioactive atoms from the filament. Approximately  $10^{11}$  radioactive atoms were evaporated in each measurement during 2 h. This means that the ion concentration in the ionization zone cannot exceed  $10^5 \text{ cm}^{-3}$ . After every measurement, the  $^{57}\text{Co}$  activity that remained in the gas cell and on the SPIG was measured. Because of the attenuation of the 122 keV  $\gamma$ -rays in the stainless steel walls of the gas cell and the unknown distribution of the radioactive atoms on the inner wall of the chamber, it was difficult to obtain an accurate value. As a lower limit, one can state that about 40% of the evaporated  $^{57}\text{Co}$  atoms diffused to the walls of the gas cell. This value did not depend on the position of the filament relative to the exit hole. The high loss due to wall collisions is in the first order not reproduced by flow calculations and could be due to turbulence induced by the filament. One-third of the evaporated  $^{57}\text{Co}$  activity was deposited on the SPIG rods and on the skimmer plate. Note that the latter value is due to ions that are not efficiently captured by the RF-structure as well as to atoms that were evacuated through the exit hole and that stick on the SPIG rods and on the skimmer plate. Measurements to decompose these two components are planned. Note that cobalt has a low-lying atomic state ( $^4\text{F}_{7/2}$ ) with energy of  $816 \text{ cm}^{-1}$ . However this state has a population of only 2% at room temperature relative to the total number of cobalt atoms. The rest of the radioactivity remained unobserved and was probably pumped away together with the helium gas.

In the case of argon as buffer gas an efficiency of 2.2% was obtained for a filament to exit hole distance of 15 mm. The amount of activity found at the walls of the chamber was a factor of 2 less compared to helium.

## 6. Conclusions

A gas cell filled with a noble gas such as helium and argon is an effective storage place for trace atoms and ions but the time scale on which chemical reactions do start to alter the state of the trace element is strongly depending on the buffer gas itself, on the impurity type and level, on the

ionization degree of the gas and on the electron density present. Also the chemical properties of the trace element itself can in some cases be of prime importance. These different time scales that have to be compared with the transit time of the atom or ion of interest in the gas cell are determining the efficiency of the whole set up. From our off-line studies we can extract a number of specifications for designing an efficient gas cell.

Although argon has a higher stopping power than helium, making it a better choice for slowing down energetic reaction products, it manifests a considerably faster bounding chemistry than helium, which could induce faster neutralization. Comparing quantitatively the relative efficiency of helium and argon as buffer gas in on-line conditions is rather complicated as the overall efficiency is a product of stopping efficiency, laser ionization efficiency and transport efficiency. Therefore a series of off-line tests were performed with  $^{57}\text{Co}$  as trace element and He and Ar as buffer gas. The efficiency for laser ionization in argon was found to be four times lower than in helium although less diffusion losses to the wall were observed. These measurements will be continued.

It is technically feasible to use a high flow rate of gas, needed for efficient stopping and a fast throughput, and still control the impurity level down to the parts per billion. But it seems hard to go below that level of purification and the main contaminant is then water. Water can easily attach to a trace ion and the time scale for such a hydration reaction lies in the ms region for the case of purified He at a pressure of 500 mbar. The binding energy of these hydrates lies in the eV region and it is possible to dissociate most of them again in the accelerating field of the extraction region. Still some elements, such as Ti for example, will efficiently set up a series of chemical reactions which lead to very stable molecules such as  $\text{TiO}$ . These molecules are hard to break and therefore the total ion intensity could be split up in a number of side bands.

A strong dependence of the dissociation process in the extraction region on the electrical field configuration and on the pressure gradient was observed. In fact the molecular ion has to gain in between two collisions enough energy in the ac-

celerating electric field to break up and the proper design of this region is critical. Due to the high density inside the gas cell, it looks impossible to prevent the formation of molecular ions or to break them up as the energy gain is less than 60 meV. Although in most cases molecular ions do not form a major problem as they later can be broken up efficiently, they could become a loss factor in the presence of electrons.

Ion–electron recombination reactions are strongly influencing the ion signal out the gas cell when electron density is higher than  $10^7 \text{ cm}^{-3}$ . Electrons can efficiently be removed by applying electrical fields inside the gas cell but at a given ion/electron density, the weakly ionized plasma will shield itself from electrical fields. The flux of incoming radioactive particles and the built up of radioactivity could lead to this threshold density. This effect will be discussed in the following paper when the presence of the cyclotron beam drastically alters the off-line observations.

A similar word of caution should be said on the use of the RF and DC electrical fields inside the high-pressure zone of the gas cell for guiding or collecting the ions.

## Acknowledgements

We would like to thank Kari Perajarvi (JYFL) and David Van den Abeele (Von Karman Institute) for calculating the flow pattern in the gas cells. This work is supported by the Inter-University Attraction Poles and the GOA Research Programs, by the Funding for Scientific Research – Flanders (FWO) and by the EXOTRAPs and the EURISOL projects.

## References

- [1] P. Dendooven, Nucl. Instr. and Meth. B 126 (1997) 182.
- [2] L. Vermeeren, N. Bijnens, M. Huyse, Yu. Kudryavtsev, P. Van Duppen, J. Wauters, Z.N. Qamhieh, P. Thoen, E. Vandeweert, R.E. Silverans, Phys. Rev. Lett. 73 (1994) 1935.
- [3] Yu. Kudryavtsev, J. Andrzejewski, N. Bijnens, S. Franchoo, J. Gentens, M. Huyse, A. Piechaczek, J. Szerypo, I. Reusen, P. Van Duppen, P. Van den Bergh, L. Vermeeren, J. Wauters, A. Wöhr, Nucl. Instr. and Meth. B 114 (1996) 350.
- [4] Yu. Kudryavtsev, J. Andrzejewski, N. Bijnens, S. Franchoo, M. Huyse, A. Piechaczek, J. Szerypo, I. Reusen, P. Van Duppen, L. Vermeeren, J. Wauters, A. Wöhr, Rev. Sci. Instrum. 67 (1996) 938.
- [5] L. Vermeeren, A. Andreyev, N. Bijnens, J. Breitenbach, S. Franchoo, J. Gentens, M. Huyse, Yu. Kudryavtsev, A. Piechaczek, I. Reusen, P. Van Den Bergh, P. Van Duppen, A. Wöhr, Nucl. Instr. and Meth. B 126 (1997) 81.
- [6] P. Van den Bergh, S. Franchoo, J. Gentens, M. Huyse, Yu. Kudryavtsev, A. Piechaczek, R. Raabe, I. Reusen, P. Van Duppen, L. Vermeeren, A. Wöhr, Nucl. Instr. and Meth. B 126 (1997) 194.
- [7] Yu. Kudryavtsev, S. Franchoo, J. Gentens, M. Huyse, R. Raabe, I. Reusen, P. Van Duppen, P. Van den Bergh, L. Vermeeren, A. Wöhr, Rev. Sci. Instrum. 69 (1998) 738.
- [8] S. Franchoo, M. Huyse, K. Kruglov, Yu. Kudryavtsev, W.F. Mueller, R. Raabe, I. Reusen, P. Van Duppen, J. Van Roosbroeck, L. Vermeeren, A. Wöhr, K.-L. Kratz, B. Pfeiffer, W.B. Walters, Phys. Rev. Lett. 81 (1998) 3100.
- [9] L.L. Weissman, A.N. Andreyev, B. Bruyneel, S. Franchoo, M. Huyse, K. Kruglov, Y.A. Kudryavtsev, W.F. Mueller, R. Raabe, I. Reusen, P. Van Duppen, J. Van Roosbroeck, L. Vermeeren, U. Köster, K.-L. Kratz, B. Pfeiffer, P. Thirolf, W.B. Walters, Phys. Rev. C 59 (1999) 2004.
- [10] W.F. Mueller, B. Bruyneel, S. Franchoo, H. Grawe, M. Huyse, U. Köster, K.-L. Kratz, K. Kruglov, Yu. Kudryavtsev, B. Pfeiffer, R. Raabe, I. Reusen, P. Thirolf, P. Van Duppen, J. Van Roosbroeck, L. Vermeeren, W.B. Walters, L. Weissman, Phys. Rev. Lett. 83 (1999) 3613.
- [11] W.F. Mueller, B. Bruyneel, S. Franchoo, M. Huyse, J. Kurpeta, K. Kruglov, Yu. Kudryavtsev, N.V.S. Prasad, R. Raabe, I. Reusen, P. Van Duppen, J. Van Roosbroeck, L. Vermeeren, L. Weissman, Z. Janas, M. Karny, T. Kszczot, A. Plochocki, K.-L. Kratz, B. Pfeiffer, H. Grawe, U. Köster, P. Thirolf, W.B. Walters, Phys. Rev. C 61 (2000) 054308.
- [12] H. Backe, K. Eberhardt, R. Feldmann, M. Hies, H. Kunz, W. Lauth, R. Martin, H. Schöpe, P. Schwamp, M. Sewtz, P. Thorle, N. Trautmann, S. Zauner, Nucl. Instr. and Meth. B 126 (1997) 406.
- [13] R.S. MacTaylor, W.D. Vann, A.W. Castleman, J. Phys. Chem. 100 (1996) 5329.
- [14] N.L. Garland, H.H. Nelson, Chem. Phys. Lett. 194 (1992) 269.
- [15] L. Lian, F. Akhtar, P.A. Hackett, D.M. Rayner, Z. Phys. D 26 (1993) S168.
- [16] C.E. Brown, S.A. Mitchell, P.A. Hackett, J. Phys. Chem. 95 (1991) 1062.
- [17] D. Ritter, J.C. Weisshaar, J. Phys. Chem. 93 (1989) 1576.
- [18] D. Ritter, J.C. Weisshaar, J. Phys. Chem. 94 (1990) 4907.
- [19] M.L. Campbell, R.E. McClean, J. Phys. Chem. 94 (1990) 8152.
- [20] L. Lian, S.A. Mitchell, D.M. Rayner, J. Phys. Chem. 98 (1994) 11 637.

- [21] R. Johnsen, F.R. Castell, M.A. Biondi, *J. Phys. Chem.* 61 (1974) 5404.
- [22] Y.-M. Chen, D.E. Clemmer, P.B. Armentrout, *J. Phys. Chem.* 98 (1994) 11 490.
- [23] S.A. Mitchell, M.A. Blitz, E.M. Siegbahn, M. Svensson, *J. Chem. Phys.* 100 (1994) 423.
- [24] B.C. Guo, K.P. Kerns, A.W. Castleman Jr., *J. Phys. Chem.* 96 (1992) 4879.
- [25] N.F. Dalleska, K. Honma, L.S. Sunderlin, P.B. Armentrout, *J. Am. Chem. Soc.* 116 (1994) 3519.
- [26] E.R. Fisher, J.L. Elkind, D.E. Clemmer, R. Georgiadis, S.K. Loh, N. Aristov, L.S. Sunderlin, P.B. Armentrout, *J. Chem. Phys.* 93 (1990) 2676.
- [27] P.R. Kemper, M.-T. Hsu, M.T. Bowers, *J. Phys. Chem.* 95 (1991) 10 600.
- [28] D. Lessen, P.J. Brucat, *J. Chem. Phys.* 90 (1989) 6296.
- [29] D. Lessen, P.J. Brucat, *J. Chem. Phys. Lett.* 152 (1988) 473.
- [30] H. Partridge, C.W. Bauschlicher Jr., S.R. Langhoff, *J. Phys. Chem.* 96 (1992) 5350.
- [31] A. Wayne Johnson, J.B. Gerardo, *Phys. Rev. A* 7 (1973) 1339.
- [32] E.W. McDaniel, *Collision Phenomena in Ionized Gases*, Wiley, New York, 1964.
- [33] P. Van Duppen, P. Dendooven, M. Huyse, L. Vermeeren, Z.N. Qamhieh, R.E. Silverans, E. Vandeweert, *Hyperfine Interactions* 74 (1992) 193.
- [34] K. Peräjärvi, P. Dendooven, J. Huikari, A. Jokinen, V.S. Kolhinen, A. Nieminen, J. Äystö, *Nucl. Instr. and Meth. A* 449 (2000) 427.
- [35] D. Vanden Abeele, Private communication.
- [36] M.M. Kappes, R.H. Staley, *J. Phys. Chem.* 85 (1981) 942.
- [37] S.W. Buckner, J.R. Gord, B.S. Freiser, *J. Am. Chem. Soc.* 110 (1988) 6606.
- [38] A. Irigoras, J.E. Fowier, J.M. Ugalde, *J. Phys. Chem.* 102 (1998) 293.
- [39] H. Ashkenas, F.S. Sherman, in: J.H. de Leeuw (Ed.), *Rarefied Gas Dynamics*, Vol. II, Academic Press, New York, 1966, p. 84.
- [40] B. Bruyneel et al., To be published.
- [41] H. Backe, A. Dretzke, G. Kube, W. Lauth, W. Ludolphs, M. Sewtz, GSI Scientific Report 1999, 107 (GSI 2000-1, March 2000, ISSN 0174-0814).